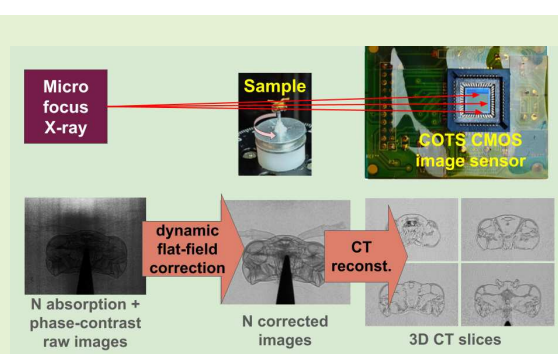


Absorption and Phase-Contrast Microtomography Using Direct X-ray Detection With COTS CMOS Sensors

Damián L. Corzi, José Lipovetzky, Fabricio Alcalde Bessia, Germán Mato, Andrés Cicuttin, María L. Crespo, Martín Pérez, Mariano Gómez Berisso

Abstract— This work presents a high-resolution X-ray microtomography system that uses commercial off-the-shelf (COTS) CMOS image sensors as direct detectors, relying on the sensor’s intrinsic resolution to achieve tomographic reconstructions without optical components. The system employs a microfocus X-ray source in cone-beam geometry, enabling both absorption-contrast and propagation-based phase-contrast imaging. A dynamic flat-field correction algorithm mitigates radiation-induced degradation during long acquisitions, helping to overcome limitations of consumer-grade hardware. The setup provides voxel sizes from $3.9\mu\text{m}$ to $5.2\mu\text{m}$. Phase contrast visualizes soft tissue boundaries that would be undetectable by conventional radiography. Compared to synchrotron or nanofocus systems, our solution is simpler, lower-cost, and avoids complex optics or slow scans. COTS CMOS sensors appear as a viable alternative for laboratory-scale high-resolution microtomography.

Index Terms— CMOS Image Sensors, X-ray Tomography, Phase Contrast, Direct Detection, COTS.



I. INTRODUCTION

COMMERCIAL Of The Shelf (COTS) CMOS Image Sensors (CIS)—originally designed for capturing visible light in consumer electronics—are an attractive option for high-resolution X-ray imaging as direct-radiation detectors thanks to their small pixel pitch, high integration density, and low cost [1]–[3]. Moreover, the small pixel pitch of CIS allows the observation of fringes caused by interference at the border of the sample, generating propagation-based phase-contrast X-ray images using just a microfocus X-ray source [4]. Propagation-based imaging enables visualization of samples with low attenuation, and can be implemented with

This work received no dedicated funding, as it was carried out during a period of austerity policies in Argentina, all experiments were done using equipment and consumables acquired previously.

D. L. Corzi (damian.corzi@ib.edu.ar), J. Lipovetzky (lipo@ib.edu.ar, corresponding author), M. Pérez, and M. Gómez Berisso are with Comisión Nacional de Energía Atómica (CNEA), Bustillo Av. 9500, Bariloche, 8400, Argentina.

D. L. Corzi, J. Lipovetzky, F. Alcalde Bessia, G. Mato, M. Pérez, and M. Gómez Berisso are with Instituto Balseiro, Universidad Nacional de Cuyo, Bustillo Av. 9500, Bariloche, 8400, Argentina.

J. Lipovetzky, F. Alcalde Bessia, G. Mato, M. Pérez, and M. Gómez Berisso are with Consejo Nacional de Investigaciones Científicas y Técnicas (CONICET), Argentina.

A. Cicuttin is with the Trieste Section of the Istituto Nazionale di Fisica Nucleare (INFN), Trieste, Italy.

M. L. Crespo is with the Multidisciplinary Laboratory, International Centre for Theoretical Physics (ICTP), Strada Costiera 11, Trieste, 34100, Italy.

a simpler setup than other phase-contrast imaging techniques [5].

In this work, we take advantage of these features to generate high-resolution tomographic 3D reconstructions from X-ray images obtained with these COTS CIS. Thanks to their ability to obtain phase-contrast radiographic images, we present CIS-based phase-contrast tomography, which offers an improvement compared to conventional absorption-contrast tomography because the phase-shift produces an interference pattern that enhances the edges of the radiographed objects. For low-Z materials, phase-contrast imaging can yield significant contrast even at low energies, where absorption-contrast techniques fail to provide sufficient information [6]. Exploiting the phase channel therefore allows observation of small, low-density samples composed of low-Z materials, while enhancing soft-tissue contrast and reducing the irradiation dose and time.

To detect interference fringes, the object must be placed at a sufficient distance from the detector, because the fringe size is proportional to the square root of the sample-to-detector distance [4], [7]. Additionally, lateral coherence is required for X-ray interference to occur; this is typically achieved using microfocus X-ray sources with focal spots of a few micrometers [7], [8]. Finally, the sensor resolution must be high enough to resolve the small fringes. These conditions can be met with a simple setup based on a commercial off-the-shelf (COTS) CMOS image sensor, as demonstrated in [4].

The paper follows with a description of the experimental

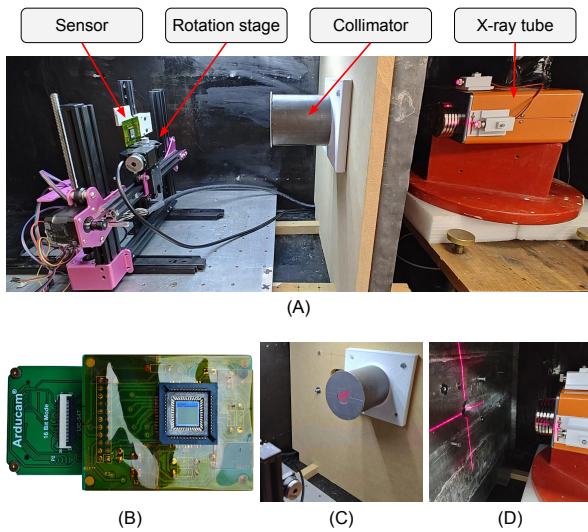


Fig. 1. Experimental setup used for tomographic acquisition (A), showing the division of the enclosure into two sections by a wall and a collimator (C). The X-ray tube was located in the first section (D), while the second contains the image acquisition system and the sensor with its electronics (B).

methods and materials. Next, the results are presented, then discussed, and finally, the conclusion is given.

II. MATERIALS AND METHODS

This section presents the experimental arrangement for the tomographies, how images are obtained and preprocessed to ensure sufficient quality to allow posterior reconstruction and how 3D reconstruction is performed.

A. Experimental setup

The experimental setup for tomography is shown in Fig. 1, where the X-ray source, sample holder and COTS CIS detector are shown. In all experiments the source-to-sensor distance was kept constant, moving the object along the system's axis to exploit both geometric magnification and phase contrast.

The entire irradiation setup was placed inside a closed, light-tight cabinet to keep the sensor in the dark. The cabinet was internally covered by a layer of at least 1 mm of lead for radiation protection. Additionally, the cabinet was divided into two sections by a lead wall with a window, which serves as a collimator. This division aims to minimize the presence of secondary photons in the detector's section of the cabinet, significantly improving the signal-to-noise ratio in the images.

The X-ray source used was a tungsten-anode Microbox Integrated X-ray Source manufactured by Micro X-ray Inc. It has a $5 \mu\text{m}$ focal spot when operated at power levels below 7.5 W, as in this work. Additionally, the tube is equipped with a 0.254 mm thick beryllium window and supports continuous operation in the 10 kV to 90 kV range, with a maximum power of 15 W.

The detector was a Micron MT9M001. This CIS consists of a 1280×1024 pixel array with a pixel size of $5.2 \times 5.2 \mu\text{m}^2$, providing a total active area of $6.66 \times 5.32 \text{mm}^2$. The small

pixel size allows the visualization of interference fringes in a similar geometry as was previously reported in [4].

The sensor readout was performed using an acquisition platform based on the UC-425 board and the UC-547 adapter, both manufactured by Arducam [9]. This platform enables sensor configuration and data readout. The complete image acquisition system is shown in Fig. 1.B, featuring the image sensor without the glass cover used to package the device. Removing this cover is essential to eliminate its attenuation, scattering, and fluorescence effects.

The readout platform was mounted 75 cm from the X-ray tube, with the readout electronics shielded with a lead layer to reduce Total Ionizing Dose (TID) effects on the Arducam board. Due to the small size of the radiographed objects, they were carefully adhered to the tip of a needle mounted on an aluminum SEM pin stub holder. The holder was placed on a Standa 8MR184(E)-11-22 rotation stage with an angular resolution of 0.015° . The stage was mounted on a motorized two-axis translation system that ran along rails, enabling easy adjustment of the object-to-sensor distance. Both the rails and the sensor holder were secured to an aluminum optical table to ensure the alignment. To reduce the presence of vibrations in the acquisition system, the optical table was placed on a low-density foam mat.

To limit the sensor temperature, a cooling device based on a Tec1-12706 Peltier cell was developed to inject cold air into the enclosure. The cold air enters the sensor section, passes through the collimator, reaches the X-ray tube section, and finally exits through an opening in the X-ray tube section, dissipating the heat generated by the system. The control of the X-ray tube, rotation stage, and image acquisition was done by an external personal computer.

The exposure time was set to 1.00 s, the sensor's maximum. Since this was insufficient to acquire enough photons to limit shot noise, multiple images were captured and averaged. The CIS analog gain was set to its maximum value. We disabled the automatic correction features typically used in standard photography [2].

B. Real-time Noise Regulation

Because exposure time and photon flux are limited, reducing shot noise requires averaging multiple one-second frames. Photon detection in CMOS sensors follows Poisson statistics; therefore, averaging improves the signal-to-noise ratio (SNR) as the square root of the number of frames. However, tomography requires many projections, which leads to sensor degradation over time due to a TID-induced increase in local dark current [10]. While post-processing can correct the mean (deterministic) component of this dark current increase, it cannot compensate for its random fluctuations (noise), which also increase with TID. Then, just increasing the number of averaged frames does not indefinitely improve image quality; an optimal number exists that balances shot noise reduction against TID-induced noise.

This effect is exemplified in Fig. 2. In the experiment, a sensor kept at constant temperature was directly irradiated with the X-ray source, and one-second exposures were acquired.

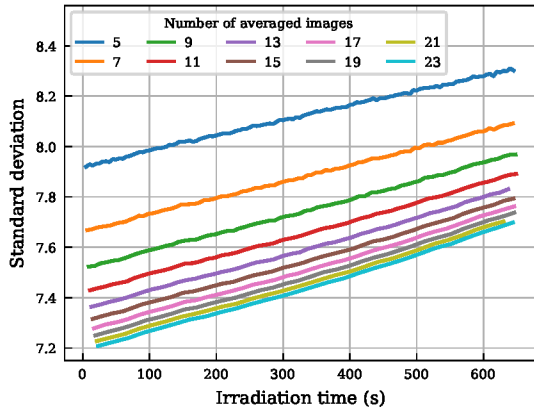


Fig. 2. Variation of the standard deviation of the CMOS sensor reading during the irradiation process, calculated for different numbers of averaged images. The plotted curves show that increasing the number of averages from 5 to 23 significantly improves the SNR.

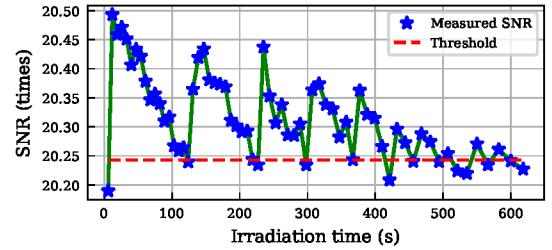
To simulate the signal that would be obtained during a long tomography at each angular position, groups of N one-second images were averaged. From each averaged image, the standard deviation was computed as a function of irradiation time; the figure plots this relationship for different values of N (i.e., different numbers of averaged one-second images); and versus total irradiation time, where TID effects become noticeable.

It can be observed that, although the irradiation temperature and photon flux are constant, the standard deviation of the pixel values increases with irradiation time and thus with TID. Maintaining a bounded standard deviation (and hence a constant noise level) requires increasing the number of averaged images as more tomography projections are acquired.

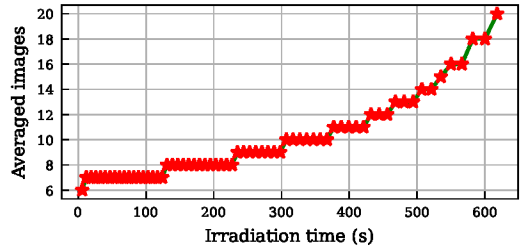
For a practical implementation of a real-time adaptive estimation of the number of averages required to obtain acceptable tomographic reconstruction, we defined an image quality empirical factor Q_{ef} as the ratio between the mean and standard deviation of an irradiated portion of an image. This empirical factor is easy to measure during irradiations, for instance, using the upper 50-row band across the entire width, which should not be shaded by the object during tomography. We proposed to maintain the value of this factor above a fixed and predefined threshold level, as a way to maintain uniform image quality along all the projections to maintain uniform noise contributions, avoiding the need for noise weighting during image reconstruction as is done in [11]. To establish an appropriate initial number of averages, this Q_{ef} value can be determined during the acquisition of the initial set of images.

The results of this implementation are presented in Fig. 3(A). Starting from an initial Q_{ef} value, the system modifies the number of averaged images to ensure that each acquisition maintains a Signal-to-Noise Ratio above a specific threshold. Fig. 3(B) shows how the number of averaged images must increase as the sensor degrades in order to compensate for this aging.

Since the number of averaged frames determines the acquisition duration at each angular position, this analysis allows



(A)



(B)

Fig. 3. Results of implementing continuous Q_{ef} adaptive regulation during the acquisition process. The system guarantees that the Q_{ef} remains above a defined threshold (A) by dynamically adjusting the number of averaged images (B).

for optimizing the sensor's lifespan by minimizing acquisition time at the start of the operation and increasing the number of averaged frames only when necessary. Finally, it is important to note that the resulting images do not correspond to equal time intervals. Therefore, the temporal distribution of the entire dataset must be stored in an auxiliary file for use during post-processing corrections.

C. Defective pixel correction and interpolated flat-field corrections

After acquisition, images are corrected for defective pixels, local pixel gain variations, and TID-induced average dark current increase in a flat-field correction, which is required to minimize artifacts in tomographic reconstruction [12], [13].

Defective pixel correction is applied in two stages. First, hot pixels (bright in the average of several dark frames) and dead pixels (dark in the average of irradiated frames) are identified. Then, each defective pixel is replaced by interpolating its neighbors. The same method can also mitigate saturated pixels. Although most cameras have built-in defective pixel corrections, this feature must be disabled since they erase single-pixel events, and the correction must be performed over averages of images to avoid this problem.

Flat-field correction is used to mitigate local pixel dark current and response non-uniformity [2], sometimes named ghosting, and is based on the acquisition of additional reference images: one obtained with the X-ray source turned off, denoted as Dark Frame (DF), and another with the sensor directly irradiated in the absence of a sample, denoted as Flat Frame (FF) [2].

However, during the acquisition of a large image set, a TID-induced increase in the average dark current implies that the correction parameters must drift over time [14]. Experimental

results showed that, to a first approximation, this increase is linear with total irradiation time. Moreover, the flat-frame response also exhibits a linear drift with irradiation time.

Assuming this linear behavior, an ad-hoc interpolated version of the flat-field correction can be applied, as described in Eq. 1. For this approach, a full set of reference images is acquired at both the start and the end of the irradiation process. These reference images are used to compute the K_D and K_F parameters, which represent the empirical slopes of the DF and FF variations, respectively, as a function of the acquired frame index i . The index i denotes the position of the i -th projection CC_i within the sequence, allowing for its interpolated correction to yield the final image IC_i .

$$IC_i = \frac{CC_i - DF_0 \cdot (i \cdot K_D + 1)}{FF_0 \cdot (i \cdot K_F + 1) - DF_0 \cdot (i \cdot K_D + 1)} \quad (1)$$

This empirical technique effectively mitigates image ghosting and the continuous increase in dark current as the sensor is irradiated during the tomography, as will be shown in the examples below in Figs. 5 and 9.

D. Application of conventional reconstruction algorithms

Tomographic reconstruction from the projection dataset was performed using algorithms implemented in the *Reconstruction Toolkit* (RTK) [15]. This toolkit includes different reconstruction methods and options, including the FDK (Feldkamp-Davis-Kress) algorithm, which is an excellent approximation of filtered backprojection for cone-beam geometries [16].

The reconstruction process begins with an image analysis, to detect the presence of any misalignment between the plane of rotation and the sensor's horizontal axis. This misalignment is easily identified through sinogram analysis and is corrected by rotating the projection set until proper alignment is achieved. However, it is important to note that rotation operations typically induce a loss of quality due to interpolation effects used to estimate the resulting pixel values. Therefore, a precise initial mechanical alignment is desirable.

After applying the reconstruction algorithms, the resulting 3D volume is typically visualized through cross-sections, enabling the observation of internal structures at different depths. Thus, a tomographic image can be generated by following the steps previously described, using a projection set derived from either conventional absorption or phase-contrast radiographies.

III. RESULTS

This section presents two examples of high-spatial-resolution tomography acquired using the system described in the previous sections.

First, we present the tomography of a packaged integrated circuit in a surface-mount package. Since this device is composed of materials with high X-ray attenuation, it is suitable for analysis using conventional absorption-contrast tomography. The inspection of encapsulated integrated circuits is of particular interest for failure analysis within the microelectronics industry.

Second, the tomography of an insect is presented. Since this specimen is composed of materials with low X-ray absorption,

TABLE I
EXPERIMENTAL PARAMETERS FOR THE ACQUISITIONS.

Parameter	Example 1	Example 2
Object	Integrated circuit	Insect
Object-to-sensor distance	25 mm	19 cm
Tube voltage - current	35 kV - 250 μ A	25 kV - 100 μ A
Additional filter	Aluminum (20 μ m)	None
Angular step	0.6 $^\circ$	0.6 $^\circ$
Phase contrast	No	Yes

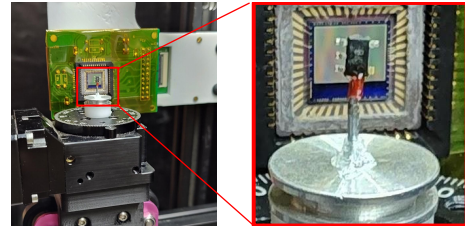


Fig. 4. Photograph of a AD8615 surface-mount operational amplifier, placed 25 mm from the sensor to obtain its tomography.

it is particularly suitable for study using phase-contrast techniques. The analysis of insects and other biological samples is of significant interest in biological research. In both instances, tomographic reconstruction was performed using the FDK algorithm, selected for its favorable balance between result quality and computational efficiency [17]. To summarize the experimental parameters used for the acquisition of these examples, the most representative values are listed in Table I.

A. Conventional absorption-contrast tomography

In this geometry, the object is placed close to the sensor, so phase-contrast fringes fall within a single pixel and are not observed. Thus, the setup is suitable for high-attenuation samples. In this position, the object magnification is negligible, and the voxel size corresponds to the pixel size of 5.2 μ m [18].

The example integrated circuit is an AD8615 surface-mount operational amplifier placed 25 mm from the sensor (Fig. 4). It consists of a silicon die connected by gold wires to metal terminals and encapsulated in plastic. To mitigate beam hardening effects in the reconstruction, a 20 μ m aluminum foil was placed at the X-ray tube output to filter low-energy photons. To compensate for the attenuation induced by this filter, the tube was set to operate at a voltage of 35 kV and a current of 250 μ A.

The results of applying preprocessing to the acquired images are exemplified in Fig. 5, while Fig. 6 displays selected projections of the integrated circuit.

After applying the reconstruction algorithms to the sinograms, the resulting cross-sections of the reconstructed volume are shown in Fig. 7. These images reveal the internal structure of the metallic chip terminals. Moreover, cross-sections (F), (G), and (H) clearly show the gold bond wires. The diameter of these wires was measured as $(18 \pm 4) \mu$ m using optical microscopy (Fig. 8). The visibility of such fine structures is particularly relevant for failure analysis in the semiconductor industry, and as a first step toward decapsulating chips for single-event effect ion irradiation in radiation testing.

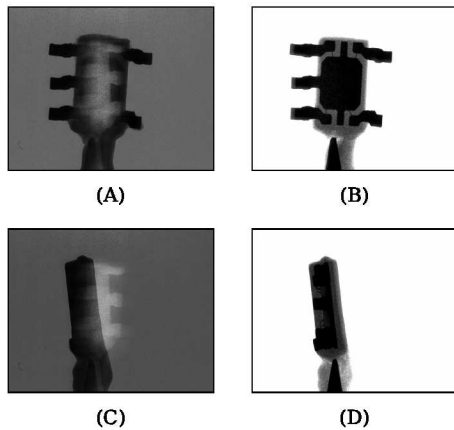


Fig. 5. Projections acquired by imaging the chip in two different angles (A, C) and results obtained after applying the defective pixel and interpolated flat-field corrections (B, D).

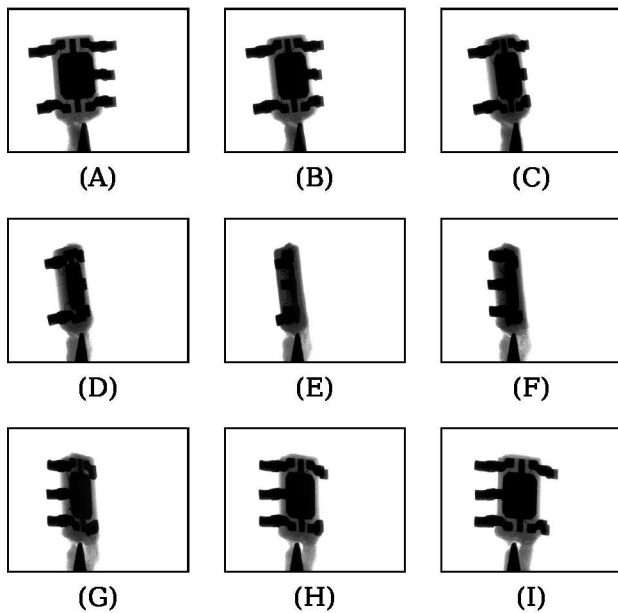


Fig. 6. X-ray images of the chip, acquired in nine different angular positions. The sequence, comprised between the first projection (A) and the last (I), illustrates the object in two positions separated by 18° of rotation.

B. Phase-contrast tomography

Phase-contrast acquisition techniques enable the observation of objects that would otherwise be impossible to visualize using X-rays due to their low attenuation. Acquiring these images requires increasing the object-to-detector distance, which simultaneously creates geometric magnification.

As an example, the head of a wasp (*Vespula germanica*) was scanned, as shown in the photograph in Fig. 9. This specimen was placed at a distance of 19 cm from the sensor to replicate the position defined in previous works [4]. At this distance, the phase-contrast fringes are stretched out and fall across different pixels, becoming visible. In this position the object has a small magnification of $\approx 33\%$, with a voxel size of $3.9 \mu\text{m}$.

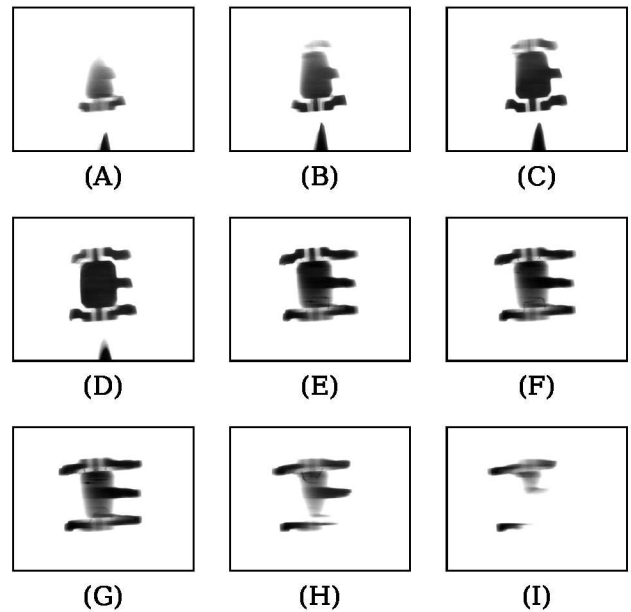


Fig. 7. Cross-sections of the reconstructed chip volume, obtained at $100 \mu\text{m}$ depth intervals, revealing the internal metal components. Gold bonding wires used for circuit interconnection, which have an approximate diameter of $20 \mu\text{m}$, are visible from image (E) to (H). Additionally, images (E) and (G) clearly resolve the ball bonds (droplet-shaped connections) where the gold wires contact the silicon die.

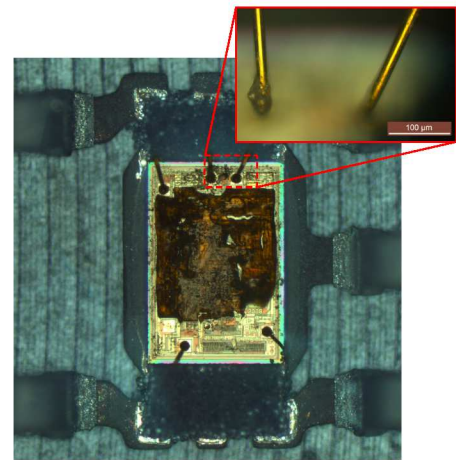


Fig. 8. Optical microscope photograph of the decapsulated AD8615 chip, showing the silicon die mounted on the lead frame and the $\approx 1.8 \mu\text{m}$ -diameter gold wire bonds.

For phase-contrast acquisitions, a softer beam is desirable; thus, the aluminum filter was not used and the source was configured to a voltage of 25 kV. The current used was $100 \mu\text{A}$. The projections obtained before and after correction are displayed in Fig. 10.

The reconstruction results are presented in Fig. 11, which shows cross-sections of the reconstructed volume. In this example, phase contrast enhances the edges of the sample, enabling tomographic imaging of a low-attenuation object that could not be analyzed using conventional absorption techniques alone. This is possible due to the high spatial

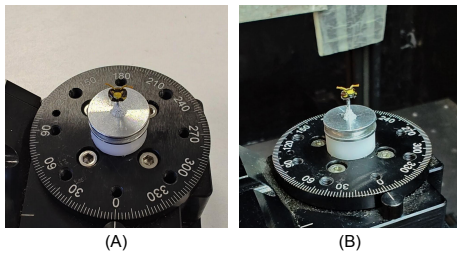


Fig. 9. Photograph of the wasp head used as a sample for phase-contrast radiographic imaging, positioned 19 cm from the sensor. The images show the mounted object before (A) and after (B) positioning the rotation stage inside the enclosure.

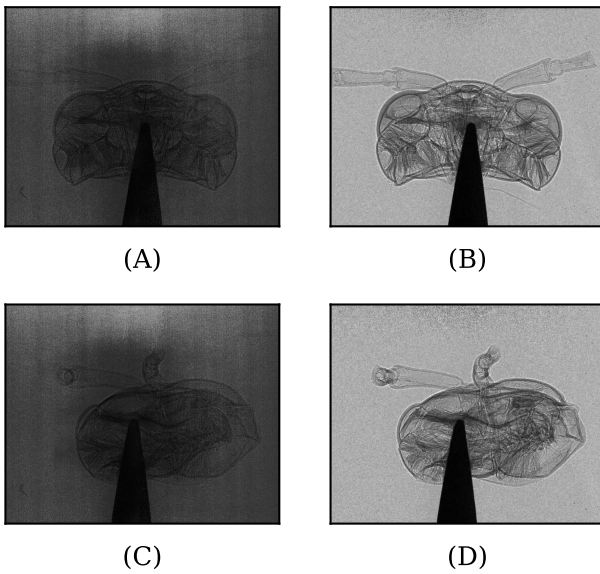


Fig. 10. Wasp head projections acquired in two different angular positions (A, C), and the results obtained after applying preprocessing algorithms to mitigate sensor degradation effects (B, D).

resolution of CMOS image sensors. However, some slices exhibit slight double-wall artifacts caused by radial clearance in the rotating stage; this issue can be avoided by using a rotation stage with higher precision and mechanical stability.

Using three-dimensional visualization tools, such as the Napari module [19], Tomopari [20], or Dragonfly software [21], the reconstructed volume can be directly visualized from various orientations, as shown in Fig. 12. These visualizations highlight the mounting needle, which represents the most highly attenuating element in the assembly.

To highlight the phase-contrast effect on the low-attenuation sample, we repeated the tomographic acquisition but placed the wasp head at only 25 mm from the sensor. In this configuration, phase effects are not manifested due to the short distance, and only absorption contrast is present in the images. Figure 13 shows six example projections acquired in this configuration. The lower contrast makes it difficult or impossible to resolve certain details, particularly in the regions corresponding to the antennae.

The reduction in contrast not only affects the visualization of the antennae but also hinders accurate reconstruction of

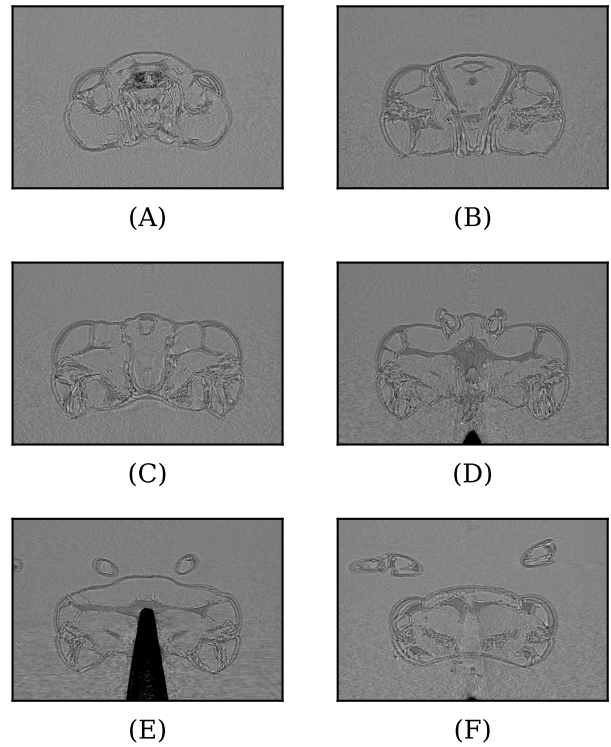


Fig. 11. Cross-sections of the reconstructed volume of the wasp head, obtained from projections acquired utilizing phase contrast.

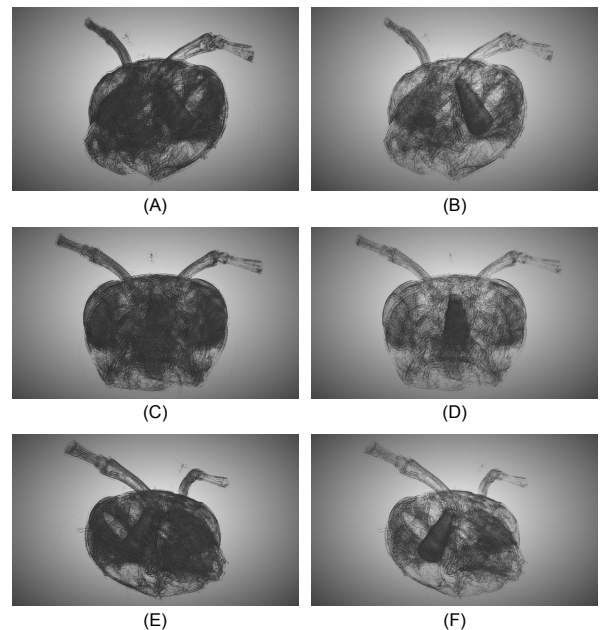


Fig. 12. Reconstructed volume of a wasp head on the mounting needle, generated using Dragonfly software. .

regions near the mounting needle used as mechanical support. This is evident in Fig. 14, where the noise level is higher in the pixel rows corresponding to the needle's position. The issue is also apparent when viewing the volume in a 3D viewer (Fig. 15), where segmentation of the wasp's head becomes

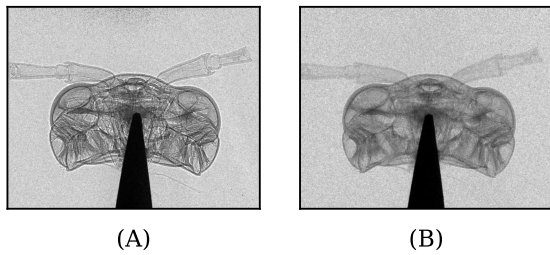


Fig. 13. Comparison of wasp head projections using phase-contrast acquisition techniques (A) and conventional absorption contrast (B). Phase effects reveal details that are impossible to appreciate using the conventional technique, particularly in the region corresponding to the antennae.

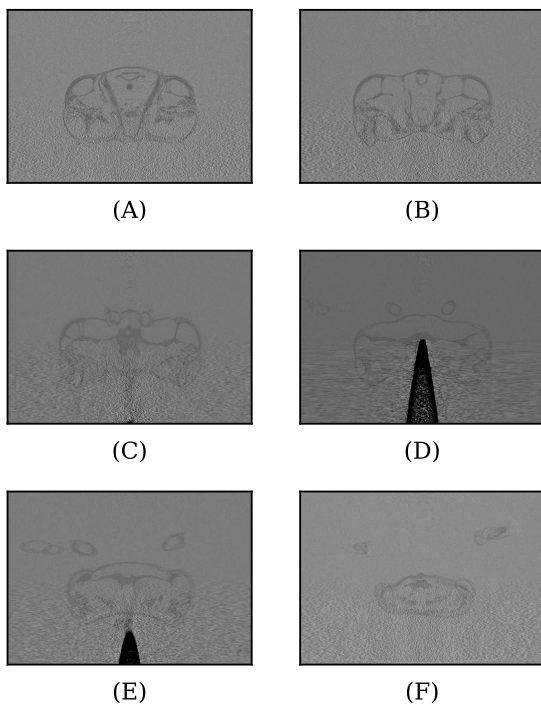


Fig. 14. Tomographic reconstruction results of the wasp head. The projections were acquired at a 25 mm object-to-sensor distance, eliminating phase-contrast contribution. Note that the rows aligned with the mounting needle exhibit higher noise levels.

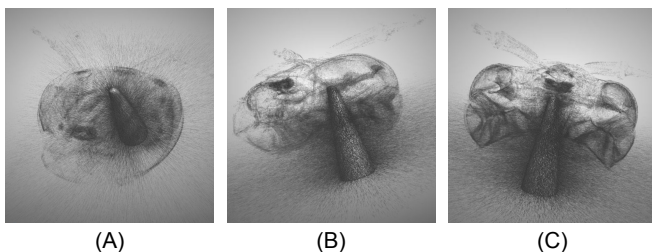


Fig. 15. Three-dimensional visualization of the reconstructed wasp head volume. Due to the 25 mm acquisition distance, there is no phase-contrast contribution. As shown, it was impossible to segment the object by applying contrast adjustments or binarization.

impossible even with contrast adjustments or data binarization.

IV. DISCUSSION AND CONCLUSIONS

This study demonstrates the feasibility of using low-cost, COTS CMOS image sensors as direct detectors for high-resolution tomography, enabling both absorption and phase contrast without the scintillators or optics that typically limit resolution. The cone-beam setup uses a microfocus X-ray source whose coherence produces interference fringes resolvable by the CMOS pixel size. The voxel size ranges from $3.9\ \mu\text{m}$ to $5.2\ \mu\text{m}$ depending on geometric magnification, allowing accurate observation of $18\ \mu\text{m}$ -diameter bonding wires.

Achieving submicrometric voxels typically requires synchrotron radiation. For instance, [22] achieved $0.9\ \mu\text{m}$ voxels with a $5.0 \times 3.5\ \text{mm}^2$ field of view, while [23] obtained $0.65\ \mu\text{m}$ voxels with a $1.3 \times 1.3\ \text{mm}^2$ field of view, extended to several millimeters for mouse brain tomography via stitching algorithms using a scientific CMOS detector. Both studies employed absorption-based tomography. More advanced phase-contrast techniques at synchrotrons, using Fresnel zone plates and high-resolution cameras, can achieve voxels as small as $15\ \text{nm}$ but over much smaller fields of view [24]. In contrast, the COTS-based system presented here offers voxels of a few micrometers over a several-millimeter field of view without requiring synchrotron access or complex optics, representing a trade-off suitable for laboratory-scale microtomography.

In contrast, nano-CT systems based on specialized X-ray sources can achieve resolutions of tens of nanometers, but they require extremely complex and expensive emitters. For example, such resolution can be obtained by focusing a scanning electron beam onto a nanometer-scale metallic anode and using geometric magnification [24]. Most of these systems rely on scintillators and complex optics to project the light generated by the X-rays onto an image sensor. Their cost is orders of magnitude higher than that of this work.

The use of much less expensive microfocus X-ray sources, as in this work, allows resolutions of a few micrometers. For instance, [25] achieved $2\ \mu\text{m}$ resolution in propagation-based phase-contrast CT using a $7\ \mu\text{m}$ focal spot, projecting images onto a scintillator coupled to a CCD via complex optics, or alternatively using geometric magnification with a Medipix detector ($55\ \mu\text{m}$ pixel pitch). Other works (see the list in [26]) employ grating-based interferometry or a modulator together with Medipix or flat-panel detectors under geometric magnification [26], but at the cost of very slow scans. Compared to these implementations, our setup offers a simple, straightforward, and less expensive configuration: a microfocus X-ray source (far more accessible than synchrotrons or nanofocus sources), no X-ray or visible-light optics, and a CMOS image sensor as an affordable direct detector. The key advantage is that the pixel size and spatial resolution of the COTS CMOS sensor are well matched to the source's focal spot and geometric magnification, providing the correct resolution for high-contrast, artifact-free tomographic reconstructions without over-sampling or under-sampling the projection data. The cost of the entire setup could be further reduced by using conventional X-ray sources (without micrometric focal spots) if only absorption-contrast images are needed.

Using CMOS image sensors for long irradiations requires

special techniques to compensate for sensor aging due to total ionizing dose (TID) effects, which increase both dark current and flat-field nonuniformities. Previously, we applied a standard flat-field correction using single reference images [2]. However, prolonged irradiations cause large variations in the correction fields, motivating the dynamic flat-field correction proposed here. We successfully implemented a modified flat-field correction that compensates for progressive sensor degradation due to accumulated dose, allowing long tomographic acquisitions. A simple linear interpolation of the correction fields proved sufficient for image reconstruction, without needing more complex approaches such as those in [27].

With all these considerations, we successfully performed computed tomography (CT) in two modes. Absorption contrast resolved internal structures as small as $20\ \mu\text{m}$ in integrated circuits, achieving a resolution better than $10\ \mu\text{m}$. Propagation-based phase contrast enabled the visualization of soft tissue boundaries in biological samples that would be undetectable by conventional radiography. These capabilities confirm that consumer-grade CMOS image sensors constitute an accessible and powerful alternative for scientific applications requiring high-resolution microtomography.

ACKNOWLEDGMENT

The authors would like to thank Julio Marin for providing the rotation stage, and the Radiation Protection Division (CNEA) assistance with radioprotection. AI tools (Grammarly, DeepSeek, Gemini) were used only as coding assistants and for English grammar correction by the non-native authors. No technical or scientific content was generated by AI.

REFERENCES

- [1] D. L. Corzi, J. Lipovetzky, and M. Gómez Berisso, "Development of an internet of things (iot) embedded open-source gamma-ray detector using cmos image sensor technology," *Journal of Sensors and Sensor Systems*, vol. 14, no. 2, pp. 197–202, 2025. [Online]. Available: <https://jsss.copernicus.org/articles/14/197/2025>
- [2] D. L. Corzi, J. Lipovetzky, F. P. A. Bessia, L. Baqué, A.-S. Sergent, M. Pérez, M. S. Haro, I. C. A. Vinciguerra, A. Martínez-Meier, G. Dalla-Salda *et al.*, "Enhanced high-spatial resolution radiographic images based on cots cmos image sensors applied to wood dendrochronology and densitometry," *Radiation Measurements*, vol. 172, p. 107085, 2024.
- [3] F. Alcalde Bessia, M. Pérez, J. Lipovetzky, N. A. Piuño, H. Mateos, I. Sidelnik, J. J. Blostein, M. Sofó Haro, and M. Gómez Berisso, "X-ray micrographic imaging system based on COTS CMOS sensors," *International Journal of Circuit Theory and Applications*, vol. 46, no. 10, pp. 1848–1857, 2018.
- [4] M. Pérez, J. Lipovetzky, L. Marpegan, M. S. Haro, J. J. Blostein, M. G. Berisso, M. L. Crespo, and A. Cicuttin, "Acquisition of phase-contrast x-ray images with commercial off-the-shelf cmos image sensors," *IEEE Sensors Journal*, vol. 25, no. 6, pp. 9618–9625, 2025.
- [5] M. Riedel, K. Taphorn, A. Gustschin, M. Busse, J. U. Hammel, J. Moosmann, F. Beckmann, F. Fischer, P. Thibault, and J. Herzen, "Comparing x-ray phase-contrast imaging using a Talbot array illuminator to propagation-based imaging for non-homogeneous biomedical samples," *Scientific Reports*, vol. 13, no. 1, p. 6996, Apr 2023.
- [6] J. Stöhr, *The nature of X-rays and their interactions with matter*. Springer, 2023, no. PUBDB-2024-05989.
- [7] C. W. Gayer, D. Hemmers, C. Stelzmann, and G. Pretzler, "Direct measurement of the x-ray refractive index by fresnel diffraction at a transparent edge," *Opt. Lett.*, vol. 38, no. 9, pp. 1563–1565, May 2013. [Online]. Available: <https://opg.optica.org/ol/abstract.cfm?URI=ol-38-9-1563>
- [8] G. Begani Provinciali, A. Cedola, O. d. L. Rochefoucauld, and P. Zeitoun, "Modelling of phase contrast imaging with x-ray wavefront sensor and partial coherence beams," *Sensors*, vol. 20, no. 22, 2020. [Online]. Available: <https://www.mdpi.com/1424-8220/20/22/6469>
- [9] Arducam, "Arducam wiki," <https://docs.arducam.com/USB-Industrial-Camera/USB3.0-Camera-Shield/Introduction/>, 2022, accessed: 2023-12-06.
- [10] F. A. Bessia, M. Pérez, M. S. Haro, I. Sidelnik, J. J. Blostein, S. Suárez, P. Pérez, M. G. Berisso, and J. Lipovetzky, "Displacement damage in cmos image sensors after thermal neutron irradiation," *IEEE Transactions on Nuclear Science*, vol. 65, no. 11, pp. 2793–2801, 2018.
- [11] G. L. Zeng and A. Zamyatin, "A filtered backprojection algorithm with ray-by-ray noise weighting," *Medical physics*, vol. 40, no. 3, p. 031113, 2013.
- [12] K. Orhan *et al.*, *Micro-computed Tomography (micro-CT) in Medicine and Engineering*. Springer, 2020.
- [13] C. C. Shaw, *Cone beam computed tomography*. CRC Press, 2014.
- [14] V. Goiffon, "Radiation effects on cmos active pixel image sensors," *Ionizing Radiation Effects in Electronics: From Memories to Imagers*, pp. 295–332, 2015.
- [15] S. Rit, M. Vila Oliva, S. Brousmitche, R. Labarbe, D. Sarrut, and G. C. Sharp, "The reconstruction toolkit (rtk), an open-source cone-beam ct reconstruction toolkit based on the insight toolkit (itk)," *Journal of Physics: Conference Series*, vol. 489, no. 1, p. 012079, mar 2014. [Online]. Available: <https://doi.org/10.1088/1742-6596/489/1/012079>
- [16] L. A. Feldkamp, L. C. Davis, and J. W. Kress, "Practical cone-beam algorithm," *J. Opt. Soc. Am. A*, vol. 1, no. 6, pp. 612–619, Jun 1984. [Online]. Available: <https://opg.optica.org/josaa/abstract.cfm?URI=josaa-1-6-612>
- [17] A. Vaniqui, L. E. J. R. Schyns, I. P. Almeida, B. van der Heyden, M. Podesta, and F. Verhaegen, "The effect of different image reconstruction techniques on pre-clinical quantitative imaging and dual-energy ct," *British Journal of Radiology*, vol. 92, no. 1095, p. 20180447, 11 2018. [Online]. Available: <https://doi.org/10.1259/bjr.20180447>
- [18] H. Villarraga-Gómez and S. T. Smith, "Effect of geometric magnification on dimensional measurements with a metrology-grade x-ray computed tomography system," *Precision Engineering*, vol. 73, pp. 488–503, Jan. 2022. [Online]. Available: <https://www.sciencedirect.com/science/article/pii/S0141635921002610>
- [19] napari contributors, "napari: a multi-dimensional image viewer for python," Zenodo, 2019, uRL: <https://doi.org/10.5281/zenodo.3555620>.
- [20] D. P. G. M. T. C. Marcos Antonio Obando, Minh Nhat Trinh, "tomopari, a plugin for accelerated tomographic reconstruction." 2026. [Online]. Available: <https://napari-hub.org/plugins/tomopari.html>
- [21] Comet Technologies Canada Inc., "Dragonfly (version 20xx.x) [computer software]," Montreal, Canada, 20XX. [Online]. Available: <https://dragonfly.comet.tech/>
- [22] M. A. Yakovlev, D. J. Vanselow, M. S. Ngu, C. R. Zaino, S. R. Katz, Y. Ding, D. Parkinson, S. Y. Wang, K. C. Ang, P. La Riviere *et al.*, "A wide-field micro-computed tomography detector: micron resolution at half-centimetre scale," *Synchrotron Radiation*, vol. 29, no. 2, pp. 505–514, 2022.
- [23] M. Humbel, C. Tanner, M. Girona Alarcón, G. Schulz, T. Weitkamp, M. Scheel, V. Kurtcuoglu, B. Müller, and G. Rodgers, "Synchrotron radiation-based tomography of an entire mouse brain with sub-micron voxels: Augmenting interactive brain atlases with terabyte data," *Advanced Science*, vol. 12, no. 28, p. 2416879, 2025.
- [24] S. Wittl, S. Zabler, J. Fell, J. Villanova, P. Lhuissier, S. Hildebrandt, and H.-G. Herrmann, "Comparing image quality of synchrotron and laboratory nano-ct scans: a round robin study," *Synchrotron Radiation*, vol. 33, no. 2, pp. 489–507, 2026.
- [25] M. Bartels, V. H. Hernandez, M. Krenkel, T. Moser, and T. Salditt, "Phase contrast tomography of the mouse cochlea at microfocus x-ray sources," *Applied Physics Letters*, vol. 103, no. 8, 2013.
- [26] C. Navarrete-León, A. Doherty, S. Savvidis, M. F. Gerli, G. Piredda, A. Astolfo, D. Bate, S. Cipiccia, C. K. Hagen, A. Olivo *et al.*, "X-ray phase-contrast microtomography of soft tissues using a compact laboratory system with two-directional sensitivity," *Optica*, vol. 10, no. 7, pp. 880–887, 2023.
- [27] C. Jaijin, J.-Y. Buffière, F. Hild, M. Poncelet, and S. Roux, "On the use of flat-fields for tomographic reconstruction," *Synchrotron Radiation*, vol. 24, no. 1, pp. 220–231, 2017.